Can grid cells produce hexadirectional signals?

Noam Almog[1,3]* Thanh Pierre Doan[2], Tobias Navarro Schröder[1,4,]**

[1]Kavli Institute for Systems Neuroscience and Centre for Algorithms in the Cortex, Norwegian University of Science and Technology, Trondheim 7491, Norway

[2]St. Olavs hospital, Trondheim
[3]Bluesky: @noamza.bsky.social
[4]Bluesky: @vitalcurrent.bsky.social

*Lead contact; Correspondence: noam.almog@ntnu.no
**Correspondence: t.navarroschroeder@ntnu.no

Abstract

Hexadirectional analysis is widely used to infer population-level grid cell activity in humans, yet this signature has not been reproduced in rodent electrophysiology, where grid cells are best characterized. Moreover, it remains unclear how grid cell populations could generate such a signal. We address this issue theoretically and empirically by evaluating three prevailing hypotheses and the null model, while critically examining the analysis framework itself. We show that the standard approach is insensitive to grid firing per se. Instead, hexadirectional modulation emerges in firing variance, which we find in ratemaps of single-cell, MEC recordings of freely moving rats. Empirically, conjunctive grid-by-head-direction tuning does not produce hexadirectional signals, whereas specific nonlinear transformations can. We argue that false positive inferences can occur and suggest approaches for improved robustness and confidence. This work has critical implications for studies on hexadirectional signals and sheds light on the neural basis of fMRI.

Keywords:

Grid cells, entorhinal cortex, hexadirectional signal, population coding, fMRI, spatial navigation, k-fold symmetry, symmetric variance.

Introduction

A central goal in cognitive neuroscience is to understand how the emergence of the mind and cognitive faculties such as memory relate to the activity of cells in the brain. One of the most successful research fields pursuing the goal of linking activity of single neurons to clearly defined cognitive variables has been that of spatial navigation. Head direction cells, mainly found throughout brain regions of the Papez circuit, are tuned to the azimuth movement direction in the horizontal plane[1,2]. While place cells in the

hippocampus and grid cells in the medial entorhinal cortex (MEC) are tuned to the spatial location of an animal[3–5]. These striking findings were first made in freely moving rodents. Linking cognitive variables of spatial location to the activity of single neurons at the top of the cortical hierarchy far removed from primary sensory areas was recognized as a breakthrough worthy of a Nobel Prize[6]. Testing the relevance of these findings for the human brain and higher cognition was hampered by the necessary invasive recording procedures. In humans fMRI has been a powerhouse of studying cognition and the brain non-invasively since the nineties[7]. However, to this day the precise dependencies of the fMRI BOLD signal to the activity of individual neurons is not well understood and remains an active area of research[8–12]. The discovery of an fMRI-based signature of putative grid-cell population activity (termed hexadirectional signal or grid-cell-like representations) during free navigation in virtual reality experiments[13] claimed that one could investigate the specific role of grid cells in higher order association cortices non-invasively in humans. It has been reported by a considerable number of independent labs[14–30], in various additional brain regions other than the entorhinal cortex, in contrast to single-unit grid recordings in rodents, and during a variety of cognitive tasks in addition to spatial navigation[14,16,19,24,28,30–32]. At the same time, however, despite best efforts some labs were not able to reproduce such effects[33].

Crucially the hexadirectional signal is a function of trajectory direction. Whether the single-unit 2D grid cell firing pattern produces the hexadirectional mean population signal remains unknown. Three main hypotheses for a potential mechanisms have been proposed[34]. H1: *Basic geometry.* The 2D grid cell pattern itself leads to activity differences across movement directions. H2: *Conjunctive cell alignment.* Conjunctive grid-x-head-direction cells have a preferred directional tuning relative to grid pattern axes[13,35] H3: *Non-linear transformation*. Grid cell firing affects the population signal in a non-linear fashion.

Using this methodology, we have provided a first-principles explanation for how the population level hexadirectional pattern arises directly from the geometry of the single cell grid pattern itself. In doing so, we demonstrate that the signal originates from the variance rather than the mean of the directional response. Furthermore, while we found some limited evidence to suggest that the directional tuning of conjunctive grid cells is anchored to the grid axes, the low specificity of this tuning makes it highly unlikely to account for the observed hexadirectional signal, consistent with our finding that the effect is absent in mean empirical activity in our dataset. We also advance theoretical understanding of the nonlinearity hypothesis through both analytic treatment and empirically grounded computational simulations. Lastly we have also provided a critical evaluation of the common hexadirectional analysis method and some of the pitfalls it can contain. Taken together, these findings bridge previously disconnected theoretical and empirical perspectives, offering a principled mechanistic account of the hexadirectional signal that refines our understanding of grid coding in humans and provides a new foundation for interpreting large-scale neural dynamics in the entorhinal-hippocampal system.

Results

To quantify k-fold rotational symmetry in a directional signal we use Fourier (like Bin Khaled et al.[35]) in a manner equivalent to sinusoidal regression in canonical hexadirectional analysis[13], where angular-frequency amplitude is a proxy for k-fold symmetric modulation (see STAR Methods). The

measure **Signal Contribution** is simply normalized amplitude (magnitude), $\hat{A}_k = A_k / \sum A$, as a percentage. **Segment activity** (firing) is the summed activity over a trajectory segment. The **directional signal** (s,θ) is either the mean or variance of segment activity for all segments sampled at direction θ, quantified for single cell, or population-level (summed) activity.

Figure 1

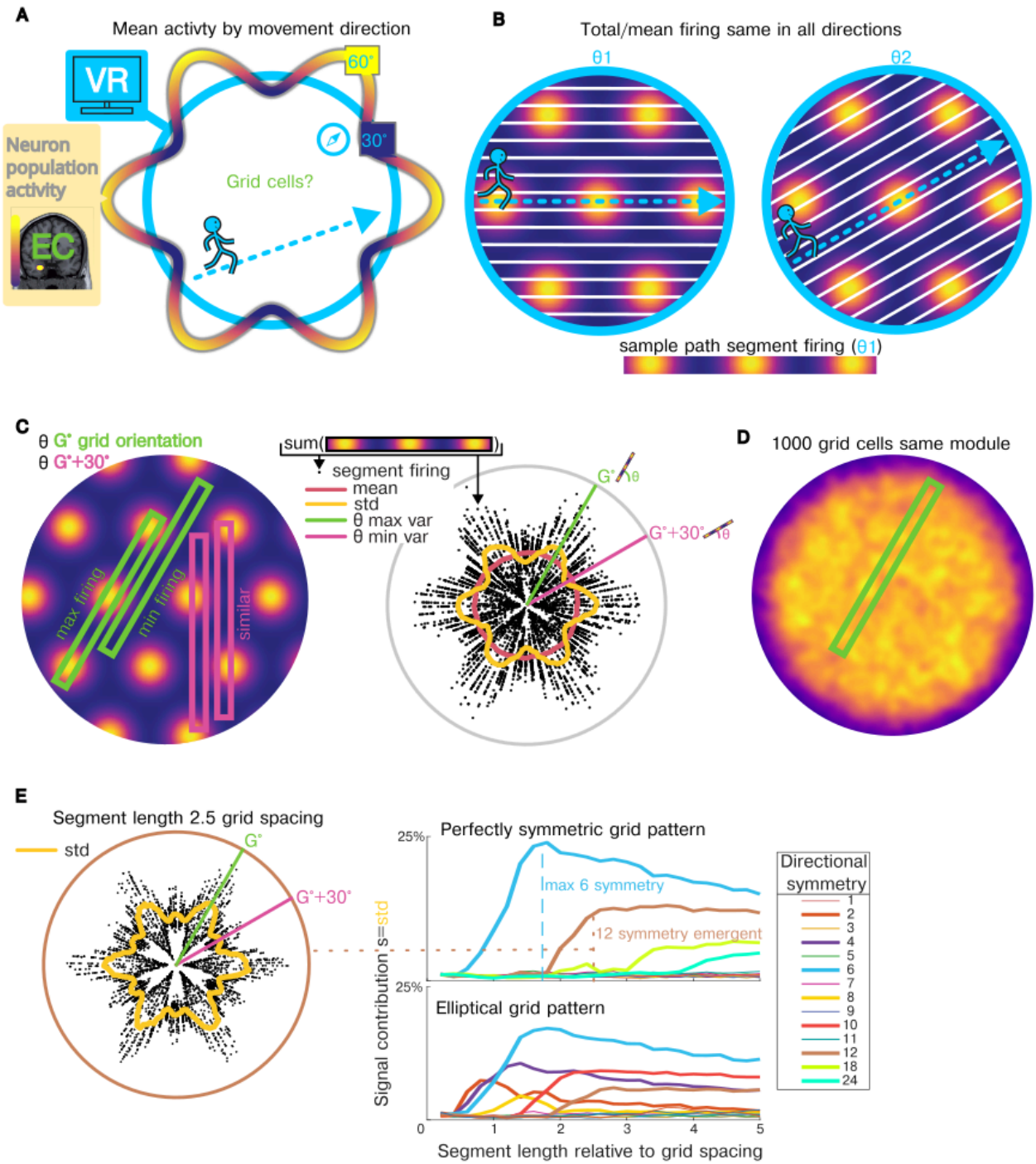

Figure 1: Directional activity produced by grid pattern tuning.

(A) Schematic of the hexadirectional signal: 6 symmetric (60°) activity peaks. Reported in human neural recordings, typically population-level, most commonly fMRI-BOLD, in entorhinal cortex while participants navigate virtual environments. Hypothesized as the signature signal of a grid cell population.

(B) When sampled completely (all locations in a 2D space), *any* spatial tuning pattern produces the same amount of mean/total activity regardless of sampling direction, because activity summed

over space is constant. Conversely, individual trajectory segment activity, like the one here containing 3 fields, may only be achievable at specific directions.

(C) Unlike mean activity per segment, **variance** is directionally modulated. For an idealized grid pattern, min and max segment activity occurs at grid orientation directions for equal segment lengths. Right: simulated segment activity over a grid pattern (equal length, black points), r-axis=activity. Note how mean is constant.

(D) A spatial tuning map produced by 1000 grid cells with same orientation and grid-espacing and uniform random phase (+ small noise). Note how contrast between high and low firing is much lower than single cell case.

(E) Effect of segment sample length on directional variance. Left: for ideal grid pattern geometry, at segment length $= \sqrt{3} * \ grid\ spacing$ two fields can be reached at both 'aligned' (grid orientation) and 'misaligned' (orientation+30°) directions (right panel, blue dashed-line). The second peak at grid-orthogonal directions produces a harmonic 12-symmetry which accounts for an increasing portion of the signal, peaking at segment length $\approx\ 2.5\ *\ \ grid\ spacing$, at which point more fields can be reached at additional directions. As segment length increases, the total energy in the signal is distributed across more harmonics. Right bottom: for an elliptical grid pattern, another set of even symmetries also account for a portion of the total energy in the signal. "Signal contribution" is the proportionate Fourier amplitude of the standard-deviation of segment activity by direction as a percentage. This approach uses polar sinusoid decomposition as a measurement of rotational k-fold symmetry, equivalent to sinusoidal regression in canonical hexadirectional analysis.

Symmetry in directional grid cell activity

Here we examine the most basic hypothesis that grid tuning pattern geometry produces a 6-symmetric directional response. For a description of how spatial/directional sampling is implemented see Methods.

Mean firing of a spatial firing pattern is not modulated by direction

To detect grid cells, hexadirectional analysis quantifies symmetry in mean directional neural response (see STAR Methods). However a major contradiction exists: principally, the mean firing of a spatially tuned cell, or population, is not directionally modulated (Figure 1B). Think of the spatial activity map as an image (color=activity). If cut into n straight parallel slices (trajectory segments), with activity meaned over slices, the mean remains constant regardless of cutting direction since the slices always partition the same total activity. Figure 1C replicates this principle with computational simulation (mean=red). Note that unlike in Figure 1B, during simulation segments have the same length. Consequently, canonical hexadirectional analysis of mean directional response, cannot detect grid cell activity (single cell, or population) from a first-principle perspective, without the presence of additional second-order phenomena.

Unlike mean, variance of activity can be modulated by direction depending on the tuning pattern. Using the image analogy again, we see that the activity pattern of a single segment may only be possible in certain directions. In figure 1B we see that having a segment containing all 3 yellow fields is possible with θ1, not θ2; only this direction contains segments with no yellow fields. Figure 1C left shows how at

grid axial directions we get both highest and lowest activity path segments. Figure 1C right, demonstrates how this produces a hexadirectional variance signal.

In large part the magnitude of this variance modulation is driven by the amount of contrast in the spatial pattern itself (the difference between high and low activity regions). While single cell grid patterns are high in contrast, when grid cells with different phases are recorded together, the contrast in the population level pattern decreases (Figure 1D). Empirically, the cells in a grid module have uniformly distributed phases[4], implying we should not expect significant hexadirectional modulation of variance in the population signal.

Segment sample length also greatly modulates the hexadirectional signal. While it is intuitive to assume that the longer the path the higher the signal, this is not the case for a pure grid pattern (Figure 1E). The segment length determines how many fields can be reached in a given direction relative to the grid spacing. Due to the 60° geometry, at a distance of $\sqrt{3} * \ grid\ spacing$, two fields can be reached at both the axial grid directions as well as the orthogonal ('misaligned') directions (+30°). This complicates the narrative that the 'misaligned' directions will have the lowest signal. In Figure 1E we see that at this length we start to see peaks every 30° producing a 12 symmetry. Figure 1E right top shows that for a pure grid pattern, lengths greater than $\sqrt{3} * \ grid\ spacing$ produce a decreasing amount of 6-symmetry as additional harmonics (multiples of the 6 symmetry) occupy a larger portion of the total energy in the signal. Noisy (empirical) and/or elliptical (Figure 1E right bottom) grid patterns will also decrease the signal. Varying segment sample lengths (as in an openfield experiment trajectory) will also lower the variance signal. Segment lengths shorter than grid spacing included in analysis only add noise, since the same number of fields (one) can be crossed in all directions.

Figure 2

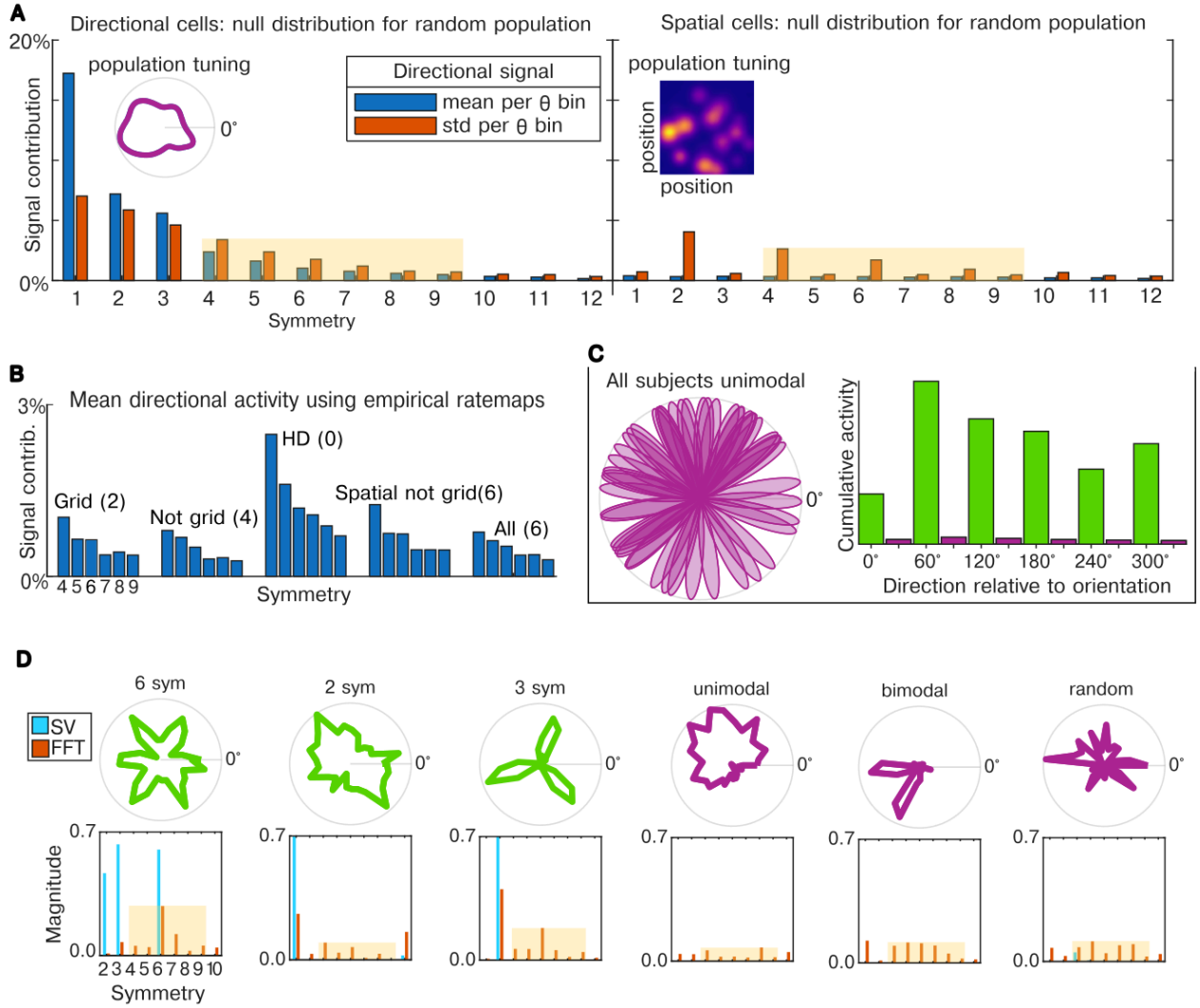

Figure 2: Null directional symmetry distributions of directionally and spatially tuned cells

(A) Null distributions for random directionally-tuned (mvl=[0.5-1]), (left) and spatially-tuned (Gaussian firing field) (right) cell populations (1-20 cells per sim). Mean over 100 monte-carlo simulations. We quantify the symmetric modulation of mean and standard deviation of trajectory equal length segments by direction using sinusoidal decomposition (See methods). Signal contribution is normalized Fourier amplitude, expressed as a percentage. Inlaid are examples of population level tunings. The subset of symmetries most often controlled against in hexadirectional analysis [4,5,6,7,8,9] are highlighted in yellow.

(B) Empirical symmetry modulation of different populations. We hybridize empirical ratemaps with simulated trajectories (see Methods) cell subpopulations from Vollan 2025 data (mean over n=29). Parentheses: n-recordings where 6-symmetry had highest signal. We show only symmetries typically controlled for in hexadirectional literature [4-9].

(C) Induction of apparent hexadirectional modulation from non-hexadirectional data. We produce a common population-level plot showing hexadirectional modulation for subjects with unidirectional response at random directions. For x-axis normalization, movement direction is

shifted by ‘mean grid orientation’ (i.e. 6th harmonic phase). Per-subject, this ‘correction’ simply shifts the activity in 360° space so peak aligns to nearest multiple of 60°, producing an apparent 6-symmetric modulation at population-level. In sinusoidal decomposition phase is largely determined by location of peaks in input, such that this occurs for most asymmetric data.

(D) Two methods for quantifying k-fold rotational symmetry. Fourier (FFT, red), which decomposes signal into sinusoids, and our method, Symmetric Variance (SV, blue), which computes cross-group variance for signal after grouping by symmetry (see Methods). Top plot: input signal. Green: rotationally symmetric signals. Signaled sampled over 30 direction bins. Gaussian noise of σ=0.2*root-mean-square(signal) added. Typical controls in hexadirectional literature [4-9] highlighted.

Null distribution of directional symmetries in directionally and spatially tuned neuron populations

The EC is also home to other directionally and spatially tuned cells than grid cells[2,36] To understand the null directional signal they produce we simulated random populations of directionally and spatially modulated cells (see Methods) in Figure 2A. We see that directionally tuned cells produce a null distribution of 1/k-symmetry modulation. Random spatial populations follow the same distribution except only in variance, and only for even symmetries (see previous results). Consequently, when these cell types are present, we expect the probability of the 6-symmetry being highest to be 2nd or 3rd highest in the 4-9 symmetry window.

We performed this analysis on empirical sub-populations in the current data[37] (23,453 cells) in figure 2B (for tuning distributions see 3B, 4C) for mean directional activity (per canonical hexadirectional analysis) using the hybrid method described (see STAR Methods). On average, pure grid cells produce neither the highest amount of 6-symmetric modulation, nor the highest number of recordings where 6-symmetry is highest (in parentheses). Overall, these resemble a 1/f noise distribution.

This also highlights the critical need to *approach this problem from a spectral analysis perspective*. Figure 2C shows a common hexadirectional plot that can be spurious (see legend), which would be clear if it were generated for multiple symmetries. We also offer an alternate measure of symmetry, *Symmetric Variance*, Figure 2D, which addresses some of the pitfalls of using sinusoidal decomposition as a proxy for k-fold rotational symmetry (see STAR Methods).

Figure 3

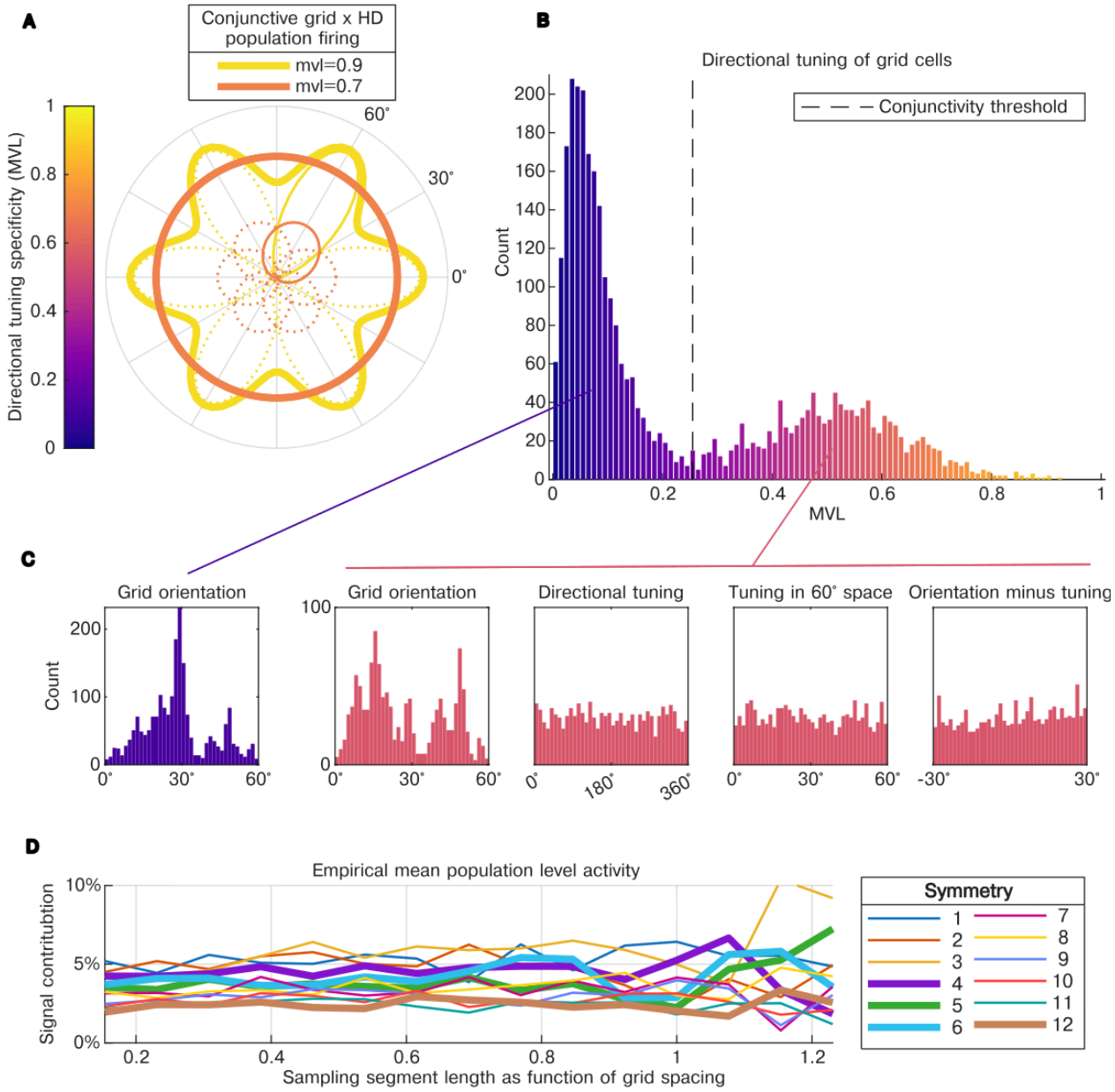

Figure 3: Directional signal of conjunctive grid x head direction cells

(A) Simulation of two conjunctive grid x head direction (grid-x-hd) populations with different tuning specificity (mean vector length, MVL). Each population consists of 6 cells with hd tuning aligned to one of 6 symmetric grid pattern directions. All cells (thus both populations) have same total firing. Individual cell firing (modeled as circular Gaussians) is shown in the thin/dotted line, combined population firing is shown with thick lines. R-axis = firing. At MVL = 0.7 directional modulation is largely eliminated. Colorbar (panels A, B, C): directional tuning (MVL).

(B) Histogram of grid cell directional tuning in dataset. Grid cells pooled across all recordings (recordings=29, grid=3699, pure-grid=2350, conjunctive=1349). We see clear bimodal

distribution between Pure and grid-x-hd cells.We also see vast majority of conjunctive cells are below 0.7 threshold required for directional modulation. Y-axis = count.

(C) Grid orientation (all recordings) pure grid cells (purple), conjunctive grid-x-hd cells (red). For conjunctive cells, relationship between grid orientation and directional tuning is also shown. While grid orientation appears clustered (different modules, animals, recordings), note difference between conjunctive and regular cells in grid-orientation distributions. Directional tuning is seemingly uniform (both in standard and 60°space ($mod(tuning,\ 60°)$). Rightmost panel: HD tuning does not align with grid axes (V-test p=0.9, V=-31), however the distribution of grid orientations minus HD tuning was not uniform (Rayleigh test p=0.03, MVL=0.05).

(D) Empirical mean population activity (averaged over recordings), sample segment length expressed as ratio to mean grid spacing for recording (Ex: segment length = 80cm, mean grid spacing = 40cm, relative length = 2). If hexadirectional conjunctive tuning was present we would expect to see a high 6 symmetry regardless of segment length. Note rats change direction frequently so n-samples decreases significantly by segment length

Conjunctive grid x head direction cells do not produce a hexadirectional signal

As shown in the previous section, a spatial grid pattern alone cannot produce a directional modulation in mean firing; for this a second-order phenomenon is required. The second hexadirectional hypothesis is that unidirectional tuning of conjunctive grid-x-head-direction cells cluster to the grid axes such that the population level firing is hexadirectional. This was reported in the original hexadirectional paper[13] for n=18 conjunctive cells across n=8 rats, but has not been replicated since as far as we know. A replication was attempted in a medical thesis project[38] in the Moser lab based on a dataset of n=224 conjunctive grid cells across 15 animals[39], which was unsuccessful.

We attempted to replicate this finding with a dataset of 29 MEC open-field recordings[37] comprising a total of 23453 cells, 3699 of which were grid cells (see Methods). Plotting the directional tuning as mean vector length (MVL), we see a very striking bimodal distribution between pure and conjunctive grid cells, figure 3B. Using the trough between the two peaks as our conjunctivity threshold (n=1349 conjunctive cells), we analyze the relationship between directional tuning angle and grid orientation with a series of histograms in figure 3C. While there are clear groupings in grid orientation as expected from grid modules derived from multiple animals (19) across 29 sessions, we see no such grouping for directional tuning, which appears to be flat (uniform) in both 360° and 60° space. To test whether head direction aligns with directional tuning grid orientation we quantify the circular distance between the two in 60° space (3C rightmost). If these two are aligned we would expect a peak difference at 0°. A circular V-test of this yields pvalue=0.9 and v=-31 indicating no significant relationship. However, for the possibility that there is an offset other than 0° we run a Rayleigh test of non uniformity, for which we get pvalue=0.03 rejecting the null hypothesis. The corresponding mean offset from the grid axes of 20°, however the MVL of this peak is only 0.05, i.e. quite flat.

To scrutinize whether there was a session-specific stable offset between head direction tuning and grid axis we ran the previous analysis on each recording individually. The mean number of conjunctive cells per recording is 47, median=15, ~5% of total, with 5 recordings having n>100 [104 116 119 130 173] ~

10% of total. For V-test of mean tuning-grid axis difference of 0°, all but 1/29 recordings did not reject the null hypothesis with α=0.05. However, the recording that did pass had the highest number of conjunctive cells of the cohort. 2 of 29 recordings rejected the Rayleigh test for uniformity at α=0.05 (MVL=0.2 for both, offset=[0°, 25°]). Notably, one was again the highest number of conjunctive cells, and the other had the highest percentage of grid cells (pure + conjunctive), 38% (next highest being 27%). Overall it appears that there is no stable relationship between grid orientation and head direction tuning, however it is compelling that the recording with the highest number of conjunctive cells, by approximately a 50% margin from next highest, did show a statistically significant Rayleigh-test result. That said, the recording with the next highest number of conjunctive cells, 130, and same percentage of population, 16%, had a V-test p-value of 0.8.

There is another subtler requirement to this hypothesis: minimum tuning specificity. Figure 3A shows an illustrative conjunctive cell population (n=6), with an ideal hexadirectional distribution of tuning, for two different tuning specificities. At fairly high tuning specificity, MVL=0.7, 6-symmetric modulation, though technically present, is negligible. Given the empirical directional specificity is MVL=0.51±0.06, it seems unlikely that conjunctive cells could generate a detectable hexadirectional signal. The recording with the highest number of conjunctive cells mentioned in the previous paragraph had a mean MVL=0.5 as did the next 4 highest.

Lastly, we examine empirical population-level mean activity in Figure 3D and compute directional symmetry by segment length. Unlike a grid spatial-tuning-response based hexadirectional signal, the grid-x-hd signal should not be modulated by segment length. Although 6-fold symmetry fluctuates, especially at longer segment lengths (most likely from sample sparsity, see next section), these fluctuations appear noise-like and do not differ meaningfully from the 1/f null (Figure 2A-left). Here we show mean modulation across recordings; for per-recording plotting see Figure 4D ‘cell mean’ (equivalent to population signal i.e. sum of cell activity).

Figure 4

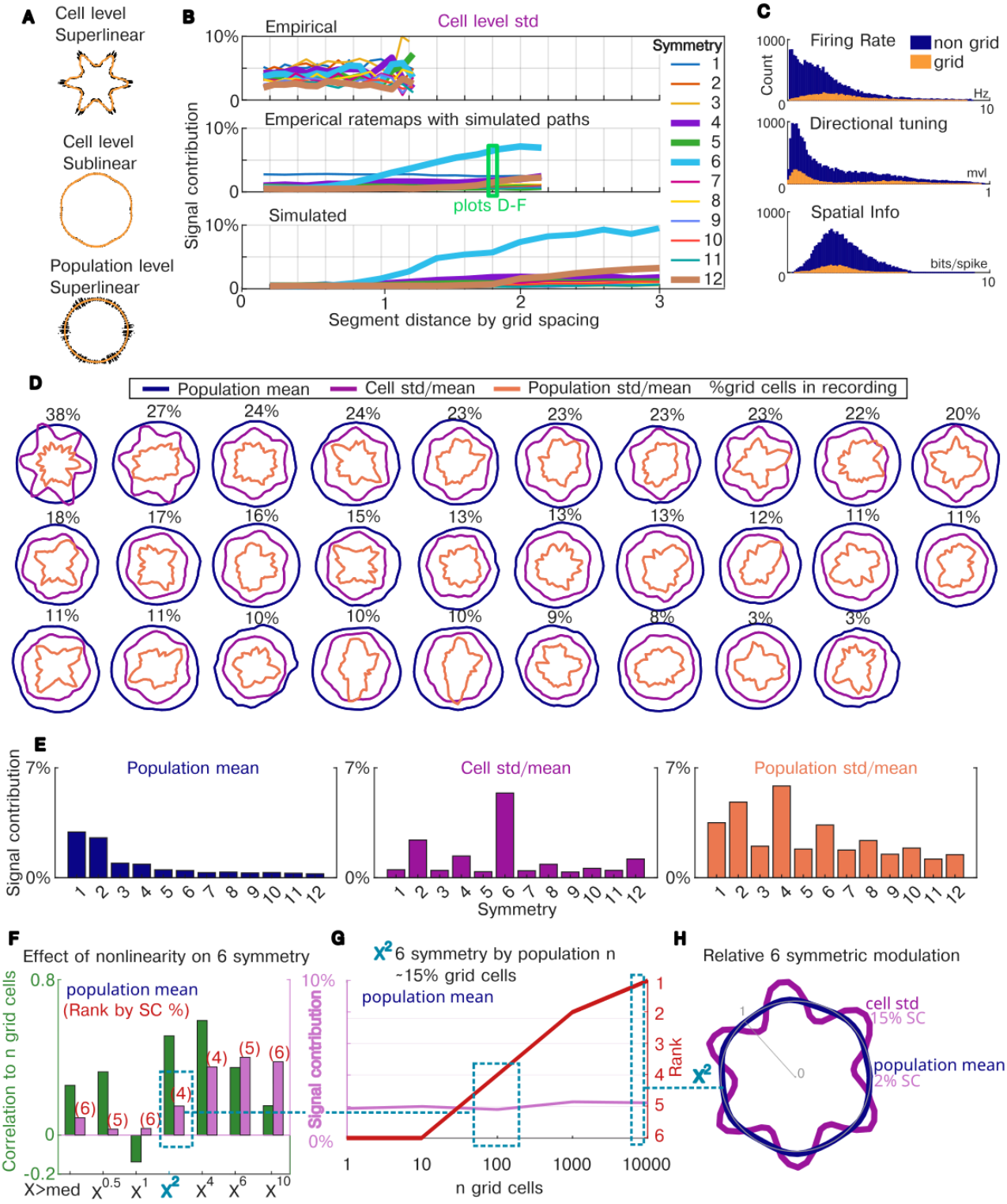

Figure 4: Directional symmetry in real and simulated grid cells, with and without nonlinearity

(A) The effect of different nonlinearities on macroscopic grid-cell activity. Plots show individual path segment with black points (θ-axis = movement direction, r-axis = population activity after nonlinear transform, mean=yellow). For each trajectory segment, we applied a nonlinearity x^c to total firing, for $c = 3$ (superlinear), $c = \frac{1}{3}$ (sublinear). Key is '*where physiologically'* the nonlinearity is applied: to each cell before summing population (cell-level), or to summed population activity (population-level). In scenarios a nonlinearity converts the uniform directional mean into a hexadirectional signal due to hexadirectional-variance produced by the grid tuning pattern (trajectory constraints discussed). Modulation magnitude differs, with the largest signal produced by a cell-level, superlinear process.

(B) Symmetry modulation in 23,453 MEC cells across 29 open-field recordings[37]. These empirical data contained a varying number of grid cells as well as spatially and directionally tuned cells, as would be expected in macro-level neural signals such as BOLD. Due to grid pattern geometry, sample segment length affects symmetry modulation. Segment length is normalized by each recording's mean grid spacing. We use three approaches to quantize cell activity: **Empirical (B top):** empirical trajectories segmented by direction and corresponding cell firing. While most parsimonious, rodents rarely run in long straight segments (excluding borders) yielding few samples at lengths where symmetric modulation is expected. **Hybrid (B middle):** using empirical spatial and directional ratemaps and interpolating new trajectories. Green-highlight: **data used for panels D-F**, segment length = $\sqrt{3} * mean\ grid\ spacing$ (theoretical length of maximum hexadirectional effect, Figure 1E). **Simulation (B bottom):** computational simulation tuned to match hybrid results extrapolated for longer segment lengths. Mixed populations of n=1000 grid, conjunctive, head-direction, spatially informative (2D-Gaussian), and noise cells at a single fixed ratio, each length simulated 100 times, mean plotted. Cell-type ratio is optimized to match hybrid data rather than the recorded proportions (see text). Notably, at n=1000 we cannot reproduce the unidirectional signal contribution (sym = 1) seen in the hybrid results. More relevant symmetries are plotted with thicker lines. "Signal Contribution" = normalized Fourier amplitude of directional signal, signal=standard deviation segment activity per direction. Polar sinusoid decomposition is a proxy for k-fold directional symmetry as in canonical hexadirectional analysis.

(C) All cells in dataset pooled. Mean firing rate (Hertz), directional and spatial tuning specificity (mean vector length, spatial information).

(D) Dataset plotted for 3 directional signals (calculated from all segments per direction): mean population-level activity (blue), mean cell-level CV (purple), mean population-level CV (orange), (CV = coefficient of variation = $\frac{std}{mean}$, % grid cells in populations). For display, signals are scaled to fit concentrically on plot (scales = [1.3x, 1x, 0.6x]). Recordings contain ~20-350 grid cells.

(E) Same data as D, contribution of directional symmetry averaged over recordings.

(F) Different nonlinearities applied at per segment cell-level activity, where maximum effect is expected. We quantify population-level mean activity (as per canonical hexadirectional analysis) for 6-symmetry only. Left-y-axis (green): correlation of signal contribution to proportion of grid cells across recordings. Meaningful 6-symmetric modulation should correlate to proportion of grid cells in recording. Right-y-axis (pink) signal contribution meaned over recordings. Red parentheses = rank of 6 symmetry by signal contribution, rank-1st = highest magnitude, over all symmetries (excluding 0 i.e. the mean). Note, regardless of nonlinearity 6-symmetry does not dominate, despite dominant 6-symmetry in cell-level variance.

(G) Scaling effect of population size on rank. We simulate a heterogeneous MEC population parameterized to match the signal contribution and rank from the hybrid approach (F) for the x^2 nonlinearity, increasing population size. This turns out to loosely match the mean empirical proportion of grid cells ~15%. While hexadirectional modulation stays constant at ~2% of total activity, the other symmetry contributions decrease such that rank of 6-symmetry increases. Blue dashed-line = hybrid data that simulation parameters were optimized for (population size, signal strength, rank).

(H) A visualization of post-nonlinearity population level mean signal contribution (2%) vs. the cell-level standard-deviation (15%) for the maximum population size (100,000 cells, ~15 % grid) for x^2, as plot G (highlighted with blue). Note cell-level activity (to calculate std) is inaccessible in human macro-level neural recording.

The nonlinearity hypothesis

Next, we tested the nonlinearity hypothesis, which proposes that a nonlinear transformation of grid cell activity produces a hexadirectional signal. The nonlinearity hypothesis bridges this by transforming the directionally modulated variance into a mean directional modulation, explaining the hexadirectional signal reported in the latter. Note that this nonlinearity must be applied to the integrated (total) firing over a path (i.e. over time), not pointwise. Our aim was not to speculate in detail about any particular nonlinear physiological processes(es) from action potential to metabolic cascades and macro-level brain recording. Our goal is instead to address this from a theoretical perspective, constraining the description of a viable nonlinearity and estimating the magnitude of the hypothetical signal.

The most theoretically likely type of nonlinearity

To produce the strongest hexadirectional response the nonlinearity is most effective at the cell-level (Figure 4A). This is because of the principle established previously that the grid pattern is most high contrast at the single-cell level and thus has the highest directional variance. In contrast, the population-level firing pattern close to uniform due to uniform distribution of grid pattern phases (Figure 2D). Similarly, relative to the scale of the original activity, a superlinear physiological process (facilitation, gain enhancement, potentiation, etc) will produce a stronger modulation than a sublinearity (adaptation, repetition suppression, saturation, etc). This can be intuited by comparing two values greater than 1 after squaring versus after rooting. We expect to see a larger difference between the values after squaring. We simulate these principles in figure 4A for a grid cell population. We see that a superlinear transformation of firing at cell-level causes the highest symmetric modulation in the mean (yellow). A sublinear nonlinearity at cell-level produces a weaker, but still visible modulation (note this is at the off-axes, i.e. ‘misaligned’), while a nonlinearity at the population level, even a superlinear one, produces virtually no modulation.

Quantifying prerequisite hexadirectional variance empirically

Working off this premise, we focus on cell-level nonlinearities. As mentioned, a prerequisite of this hypothesis is hexadirectional variance. To begin, we verify that this variance pattern exists empirically. As discussed the spatial-tuning-hexadirectional-signal is caused by varying distance required to cross

consecutive firing fields at different directions. This requires having straight trajectory samples of lengths at least close to grid-spacing. A central problem in investigating the hexadirectional signal with rodents is that in open environments rodents rarely run in long straight lines except along borders. Critically, this alone could explain why the hexadirectional signal has not been reported in rodents. We nonetheless analyzed the variance modulation directly in our rodent data (Figure 3B top), which does not show 6-symmetric variance modulation, even at segment lengths predicted in simulation (3B bottom). However, we could not preclude that this was due to decreasing number of samples at longer lengths.

Hybrid approach

Despite continually adding parameters to our computational model (20+ parameters) including: elliptical grids, field location noise, see Methods), we could not replicate the unique empirical distributions of spatial and directional cell-tuning (Figure 4C). To remedy this, as well as the lack of longer segment samples, we used a simple hybrid approach for bootstrapping new data: treating the empirical spatial and directional ratemaps of each cell as joint independent marginals, and sampling new segments (see Methods). Note: our segment lengths were still constrained by the arena dimensions relative to the empirical grid spacing.

Figure 4B shows a Fourier decomposition of directional firing for three sources of data: empirical, hybrid, and simulated. We measure the mean cell-level standard deviation over segment activity per direction, as we expect the highest hexadirectional signal. We use standard deviation, not variance, to stay in the same relative scale as the original signal, as this is what will be input into any downstream nonlinear process. The mean over all recordings is shown. From these plots we estimate that a sampling segment length of at least ~1.3 times the mean grid spacing is needed for a reliably dominant 6-symmetric signal. According to the hybrid data this modulation is around 6% of the total standard deviation of the signal. According to the simulation this could increase up to 10% at greater lengths. Interestingly we do not see the theoretical signal peak at *sqrt(3)*grid-spacing* as in figure 2E, this is likely due to having non-grid cells in the population, reducing overall signal, (note difference y-axis limits). That said we do see that the 12 symmetry increasing in magnitude. To compare other aspects of the signal, we fix segment length *sqrt(3)*grid-spacing*. Besides the reasons mentioned, this length was obtainable in most recordings. This segment length is used for the analysis.

To better understand the distribution of symmetric modulation in this dataset we have plotted 3 directional signals for each recording individually (4D), with mean plots in 4E. We use the coefficient of variance, CV, $\frac{std}{mean}$, to account for mean fluctuations that are theoretically unrelated to spatially firing, and to maintain relative scale to overall signal magnitude, important when considering detectability. Cell-level CV (purple, 4D) shows clear correlation between grid-cell proportion and hexadirectionality, implying causality. At the aggregate level, we see a dominant 6-symmetry at ~5% of the total CV (4E), despite the empirical noise of a mixed directionally/spatially-tuned cell population (4C). Though partially extrapolated*, this is the most empirical evidence of a rodent hexadirectional signal that we are aware of.* As predicted, mean activity (blue) has little directional modulation, and generally resembles the 1/f null distribution of random directional signals (Figure 2A-left, Supplementary Figure S1A). Both cell and population level variance (4E, purple/orange) show the hallmark of spatial-tuning-derived directional activity where even symmetries are elevated (2A-right). The population-level variance resembles a null

spatial tuning distribution though 4 and 2 symmetries are inverted. However, when viewed individually, the population-level variance signal has unexpected structure; not hexadirectional, but clearly modulated by direction: aligned to grid axes at times, and orthogonal at others, with the highest symmetry being 4-fold, in contrast to the null distribution.

Applying a nonlinearity

Given we detected hexadirectional modulation in cell-level variance, we explored some basic nonlinearities on cell-level activity (4F, 4G). We quantify only 6-symmetry (segment length= $\sqrt{3} * gridspacing$, hybrid method). Maximum correlation of modulation to grid-cell proportion (left-axis, green, across-recordings) occurs at x^4; with minimum at x^1 (no transform/nonlinearity), as expected. Comparing magnitude (right y-axis) we see max of 5% (x^4, x^6, x^{10}). In red we show rank by magnitude across all symmetries (1st=highest i.e. dominant), which more clearly contrasts against the null distribution. We see peak rank=4th for x^2, x^4. Consequently we consider x^2 the weakest nonlinearity to produce the highest signal, based on raw magnitude. 6-symmetry rank=4th, while not dominant, is higher than chance for non-grid directional populations (6th), though lower than chance for random spatial ones (3rd) (Figure 2A, Figure S1A-rightmost). x^2 has significance in nonlinear natural processes as a_2x^2 is the lowest-order nonlinear correction to a linear model ($a_0 + a_1x$). We focus on x^2 in figure 4G. The sublinear transform we tested, $x^{0.5}$ appears to not produce a detectable signal. The thresholding nonlinearity, $x \leftarrow \{0, x < median(x)\}$, was also non-viable. Higher thresholds may work, but may also be susceptible to noise similar to high exponents seen here.

Scaling effect

So far applying nonlinearities did not produce strong evidence for a detectable hexadirectionality in macroscale signals like fMRI-BOLD: 0-5% modulation, rank close to chance, for ground-truth signal. However, a decisive scaling factor is captured by rodent data. For smaller MEC populations, sparse amounts of directionally, or spatially tuned cells produce anisotropical patterns that are more disruptive to a symmetric modulation. In larger populations of the same cell-type proportions, the directional and spatial noise from non-grid cells will ostensably become uniformly distributed. Though our empirical data contains populations of $n \approx 1000$ cells, we can simulate up to 1 million (see Methods). To test scaling, we parameterized our simulations to produce the mean signal curve of the hybrid approach and increased the population size (Figure 4G). We see that while hexadirectional signal magnitude remains at 2%, its rank increases. Though seemingly contradictory, this signifies that while 6-symmetry magnitude relative to overall mean signal remains the same, the noise-based symmetries decrease. Importantly, his effect relies on uniformly distributed spatial and directional cell tuning. Exploring the scaling effect across nonlinearity exponents, unexpected optimality exists for exponents between [$x^{1.5}$, x^3], with signal strength peaking at around 2% and dominant symmetry occurring at ~10000 grid cells Figure S2.

Discussion

We tested the hypothesis that grid cells produce a hexadirectional signal observable at the macro/meso-scale (fMRI, MEG, iEEG). Despite the widespread application of hexadirectional analysis, a clear account of how grid cells produce this signal has been lacking. To address these gaps, we evaluated the three leading hypotheses[34,35] using largescale rodent grid cell recordings[37], and computational simulations.

We have shown that based on first principles and empirical data, grid cell firing alone does not produce a hexadirectional signal in mean directional response: the quantity measured in the literature. In terms of hypotheses relying on additional phenomena to produce a mean hexadirectional signal, while we found marginal evidence that the directional tuning of conjunctive grid cells is anchored to the grid axes, the low specificity of this tuning argues against this explanation. While a number of non-linearities may underlie the neurovascular coupling of the fMRI-BOLD signal[40–44] this remains an active field of research[9,12,43,45]. Regardless, we have shown theoretically that the nonlinearity hypothesis is viable and have identified its most likely physiological description: a cell-level, superlinear, relatively weak ($\sim x^2$) transformation of path segment firing. If combined with an increased number of grid cells contributing to the population signal (~10k+), a small but dominant hexadirectional signal emerges from the ground-truth, single-cell data: ~2% hexadirectional modulation of mean directional response for a heterogeneous MEC-like population (Figure 3F-H) (note this dataset does not include interneurons which could inflate the signal we estimate). Regarding the number of neurons in the human EC estimates range between 5-15k cells per mm^3 depending on layer and location[46–48]. For a $3mm^3$ voxel this would correspond to 135-405 k neurons. In rodents grid cells can exceed 30% of all recorded MEC cells[36]. Thus their count could exceed 120k+ cells in a $3mm^3$ voxel, which would support the scaling effect mentioned above, though this is using most favorable estimates and assuming appropriate sampling of the pmEC (human homologue of rodent MEC with a volume of ca. $600mm^3$)[49–52].

Note that in addition to selecting a segment length optimized to grid-spacing (Figure 1E right, 4B), to produce a hexadirectional signal we apply a nonlinearity to the neural activity of each segment individually; there is no continuity in time. While mathematically expedient, this implies a precise, directionally-gated physiological mechanism. Alternatively, our results would reflect a time-based nonlinearity (superlinear) for trajectory segments matching the time constant. Varying speed and segment length adds significant noise to an arguably tenuous hexadirectional signal. We did not systematically address the impact of different sources of noise, such as physiological, analysis or measurement related, as it goes beyond the scope of our proof-of-concept approach. In the same vein, we did not include human fMRI data, because we assumed a ground-truth, single cell perspective.

Assessing the null hypothesis, we have highlighted pitfalls in hexadirectional analysis (see STAR Methods). Namely, computing a single harmonic decomposition without contextualizing using spectral analysis. We have generated the null distribution of symmetric directional modulation for random populations of directionally and spatially tuned cell populations (Figure 2A). We have shown that in commonly used control symmetries, a dominant 6-symmetry is 3rd or 2nd highest by chance, and that

pre-processing can affect false-positive statistical inference (Figure S1). We have also shown that a popular, group-level plot of the hexadirectional effect easily results also from random data (Figure 2C).

The MEC is also home to other directionally tuned cells[2,36] Unlike pure grid cells these cells are defined by the strong peaks they produce in directional firing. Consequently, these neurons will have large impact on directional analysis. We have shown how sinusoidal decomposition is not an ideal proxy for measuring rotational symmetry and can yield unreliable symmetry estimates (Methods, Figure 2D, Figure S1). Specifically, we have shown that directional activity peaks produced by cell-types such as these produce high, temporally stable measures of symmetric modulation (Figure 2A, Figure 2D, Figure S1D, STAR Methods).

A compelling case for the hexadirectional signal is the replicated observation that it correlates with behavioural performance[13,21,53] in fact stable *non*-symmetric directional activity from *non*-grid cells that is being reported in these studies, it would still explain the correlation between navigation circuitry and cognitive performance. As shown, this non-symmetric but *stable* directional activity would have a reasonably high chance of passing controls in hexadirectional analysis (partitioning data, non-zero mean, and naive shuffling, Figure 2A, Figure 2D, Figure S1A, Figure S1D, STAR Methods).

A major difference between human grid cell research and the rest of the grid cell field is that the effects in hexadirectionality are commonly only statistically tested at the group level, with simultaneously very few clear single subject examples of the hexadirectional signal. Arguably this indicates that hexadirectional analysis is currently not reliable enough for subject-level clinical applications. Another idiosyncrasy is that positive results often only occur after dividing the data into specific subsets: e.g. by behavioral state, task epoch, participant group, or (sub)frequency band. If these subdivisions were standard across studies this would not be an issue, but collectively, these post-hoc subdivisions inflate the Type-I error rate. These issues have been discussed in the broader context of the replication crisis[54,55].

Complementary computational work[35] directly addresses these same three hypotheses. This work also reports a nonlinearity-based hexadirectional signal, in this case with time-based sublinear transformation (i.e. adaptation/repetition suppression). However, this effect disappears for shorter paths and decay constants that do not precisely match movement speed with grid field spacing. Even in ideal (non-empirical) conditions, the effect is only marginally above noise-level. Unlike us, this work reports mean hexadirectional signal from grid cell activity alone. The effect reported is small, only occurs for "star-like" trajectories, and is "strongly dependent on the subject's starting location relative to the locations of the grid fields." By far the strongest hexadirectional signal reported in this work arises from the conjunctive cell hypothesis, contingent on high directional specificity and tuning direction clustering parameters. Notably these parameters are drawn from older, smaller studies[13,56–58] and were not replicable in the current, larger dataset[37]. The authors further noted that the effect is the same if non-grid directionally tuned cells were hexadirectionally clustered. Notably, they identify a false-positive artifact stemming from trajectory geometry, an important consideration for open-field and/or experiments with asymmetrical/irregular directional sampling.

It is noteworthy here to mention the parallel between this line of work grid cells in 1D linear track environments. In both contexts the 2D grid pattern is collapsed to 1D. In particular, previous work[59]

described sampling the 2D grid pattern in straight paths at different directions. This work focuses on single-cell-level activity in fixed directions, while we focus on the overall directional modulation at the population-level, we nonetheless arrive at many of the same findings. Just as importantly, we converged on the same analytic methodology of using Fourier for this problem[59].

To bolster the hexadirectional hypothesis going forward we recommend quantifying stable directional activity peaks as standalone effects, significant in their own right. For detecting grid cells non-invasively we also recommend measuring directional variance, though we predict a small signal at the population/macro-level. Notably, in this study we showed a hexadirectional variance pattern only with extrapolated trajectories. It would be ideal if hexadirectional variance were shown empirically with rodents running longer (straight) paths. To bolster the physiological basis of the nonlinearity hypothesis, more research on neurovascular coupling is needed. To consolidate observations across studies more standardization is needed[60]. Simple, individual level plots with minimal pre-processing (direction vs activity) should ideally be reported in addition to group level second-order statistical plots to build a better intuition of the typical directional signal.

Here, we demonstrated critical limitations of hexadirectional analyses in detecting grid cell population activity, as well as the merit of this approach under different hypotheses. This work has further implications for bridging single-cell activity to population signals like fMRI-BOLD in the EC and beyond.

Resource availability

Lead contact
Requests for further information and resources should be directed to lead contact, Noam Almog (noam.almog@ntnu.no).
Materials availability
NA
Data and code availability
Available upon publication

Acknowledgments

We are grateful for helpful discussions with Yoram Burak, Jan-Mathijs Schoffelen, David Attwell, Noam Shemesh, Ila Fiete, Michael Hasselmo, Jeffrey S. Taube, Dori Derdikman, Martin Stemmler, Andreas Herz, Richard Kempter, Neil Burgess, Christian Doeller, Yasser Roudi, Ines Samengo, Patrick J. Drew, Omri Barak, Ikhwan Bin Khalid and help from Natalie Ruth St. John.
We thank Abraham Vollan and Edvard and May-Britt Moser for providing the rodent data. The work was supported by two Research Council of Norway Centre of Excellence Grants (Centre of Neural Computation, Grant number 223262; Centre for Algorithms in the Cortex, Grant number 332640). In addition, the project was funded by the Kavli Foundation.

Author contributions

NA, Conceptualization, Data curation, Software, Formal analysis, Investigation, Visualization, Methodology, Writing. TPD, Conceptualization, Methodology, Writing. TNS, Conceptualization, Resources, Supervision, Funding acquisition, Methodology, Writing.

Declaration of interests

The authors declare no competing interests.

Declaration of AI technologies in the writing process

The authors used ChatGPT, Claude, and Gemini for paraphrasing and grammatical corrections. The authors take full responsibility for the content of the publication.

Supplementary Material

Figure S1

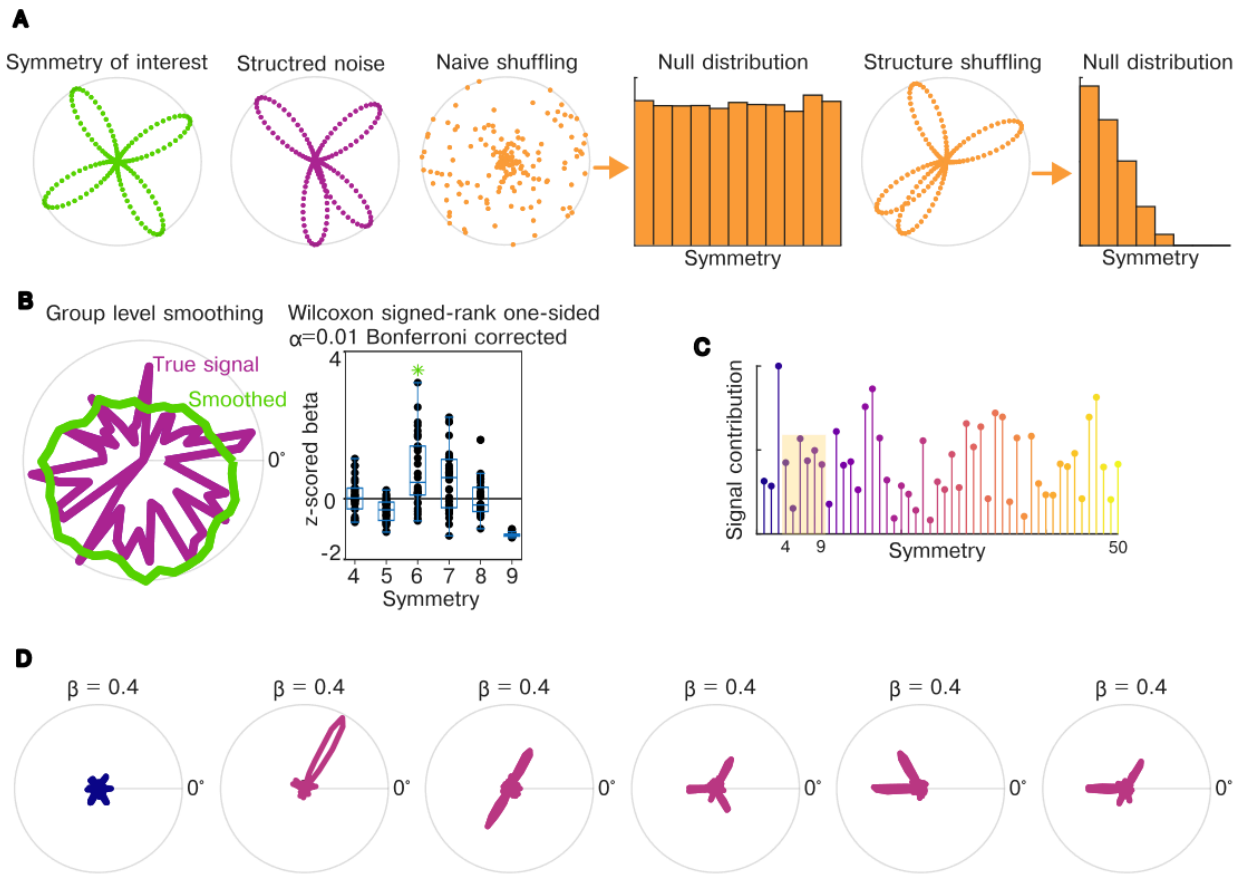

Supplementary figure 1: Pitfalls in hexadirectional analysis

A. The importance of shuffling the correct feature of data. In this example we are testing for a 4-fold symmetry in data composed of 4 random directional peaks. In the first case we assume a null hypothesis where bin values are independent of each other. This naive shuffling of bin labels produces a uniform null distribution of symmetries. In the second case we assume an underlying structure to the data where nearby direction bins are correlated and thus shuffle peaks spanning multiple bins. This results in a much different null distribution of symmetries[61].
B. An illustrative simulation showing that optimizing parameters in the data processing can create a statistically significant results from noise. Here we simulate the data for 30 subjects sampled in 60 direction bins with uniform random numbers. We use a moving average to smooth the data, however we select window size to maximize 6 symmetric modulation at the group level. We then test statistical significance of the hexadirectional signal. This process achieves statistically significant hexadirectional modulation from random data frequently (every 1-3 simulations).
C. An illustrative plot showing that hexadirectional analysis typically only controls for a very small subset of possible directional symmetries [eg, 4-9], instead of the full spectrum (as limited by

directional sampling precision). This is of concern because the lower number of control symmetries, the higher the chance of false positives. This plot shows the directional symmetry modulation for a random directional signal of 100 direction bins, note the variance in signal contribution amplitudes.

D. Misleading β's. An illustrative example of a pitfall related to quantifying hexadirectional signal with unbounded regression coefficients. In this example each signal has the same total energy (total firing), note r-axis magnitude. While the first case is truly hexadirectional, the rest are not, yet all produce the same regression coefficient.

Figure S2

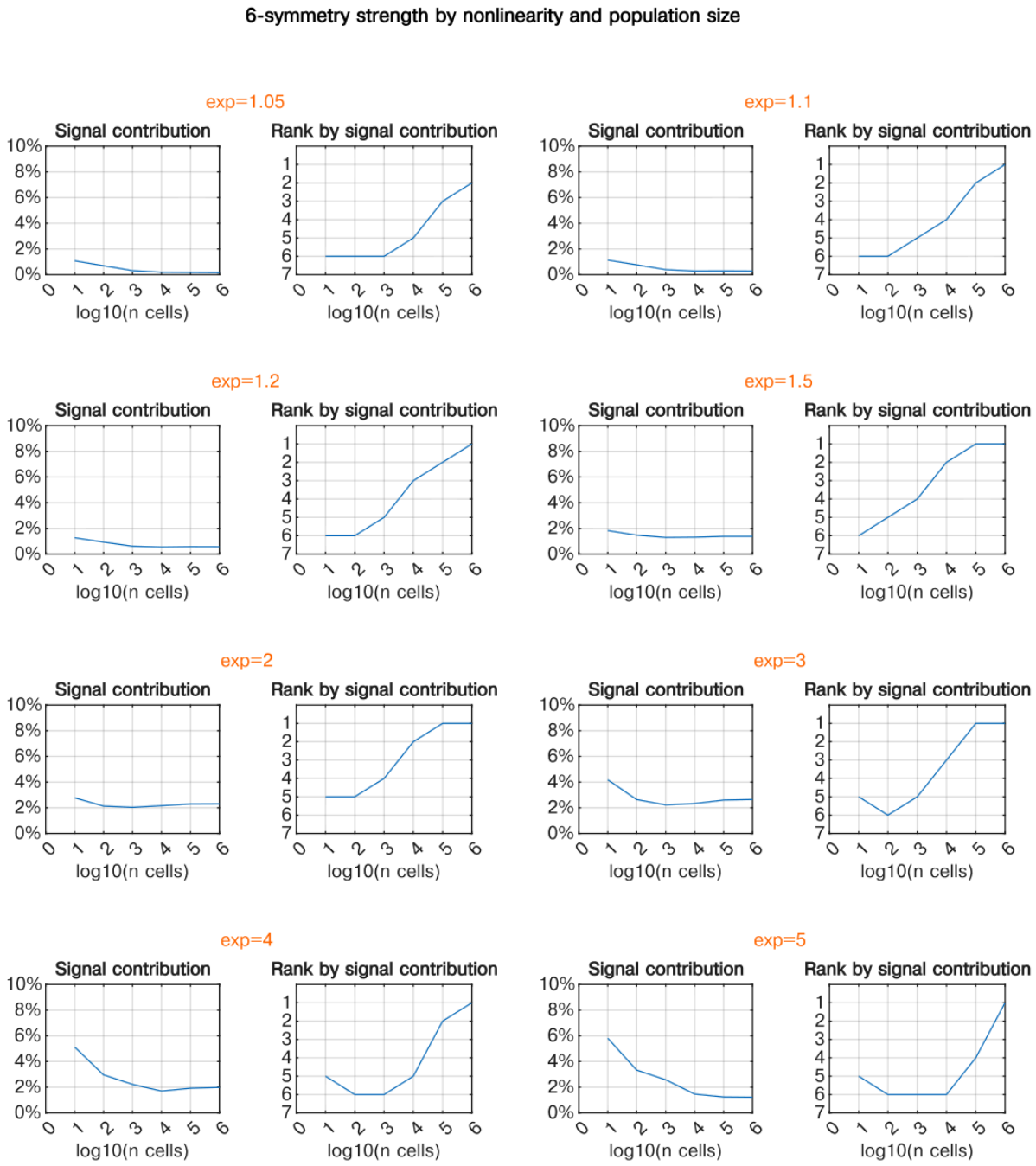

Supplementary figure 2: Effect of nonlinearity power and MEC population size on hexadirectional modulation. Here we explore two parameters, nonlinearity strength, and population size on hexadirectional modulation using Monte Carlo simulation (100 simulations per population n). The same as Figure 3G but for additional exponents (see corresponding legend). Notably in this plot x-axis is expressed by the size of the total population, of which grid cells are roughly 15%. We also extend the simulation up to 1 million cell populations. Interestingly we see signal contribution at large populations

first increase and then decrease as nonlinearity power increases (note: this is a subtle effect). The same appears true for rank (only intermediate nonlinearities each rank 1 at population size $n = 10^5$ cells). Decrease in signal in the larger nonlinearities is likely due to decrease in anisotropic directional noise as directional noise becomes more uniformly distributed, removing energy from other symmetries, simultaneously as the 0 symmetry (mean, which is not removed from the signal during analysis, see Methods), the majority of the signal, increases nonlinearly with population size. This is supported by the fact that though the signal is high at low population sizes, the rank is not, indicating that all symmetries are higher relative to the mean.

STAR Methods

Vollan 2025 dataset

This dataset contains electrophysiological recordings from 19 freely behaving rats implanted with high-site-count Neuropixels probes in the medial entorhinal cortex (n=10), the hippocampus (n=2), or both regions (n=7). Numbers of simultaneously recorded units ranges from 235-1,522 and included all cell types except interneurons. For this study we did not use the hippocampus only recordings. Of the different navigational tasks, we only used the open field sessions for a total of 29 recordings (n=18 rats). These rats foraged for randomly scattered food crumbs (corn puffs or vanilla cream cookies) in a square open-field box with a floor size of 150 × 150 cm and a height of 50 cm. The floor was made of black rubber, and the walls were made of black expanded PVC plastic. Notably one of these openfield sessions occurred in a darker lit, circular environment 150cm in diameter. This recording was not remarkable in any statistical way we observed 6th highest grid cell account, etc, so we did not exclude it from the dataset. The animals' head positions and orientations were tracked with OptiTrack motion-capture system. The raw neural activity was spike-sorted using Kilosort 2.5. Cells with mean spike rate of less than 0.1 Hz or greater than 10 Hz were excluded. For a more detailed description see[37].

Quantifying rotational symmetry

Hexadirectional analysis has multiple implementations; here we focus on the most common approach: 6-period sinusoidal regression. Nonetheless, the majority of this discussion applies to other implementations such as Representational Symmetry Analysis (RSA).

Hexadirectional analysis disambiguation

The most common hexadirectional analysis method is a form of circular regression where the 6 harmonic modulation (60° periodicity) is calculated (Eq. 1 below). In terms of nomenclature this is technically multiple regression, and thus it is technically a General Linear Model (GLM) and also a Generalized Linear Model (also GLM).

In the context of hexadirectional analysis the phase of the 6 frequency component is dubbed 'mean grid orientation' and magnitude (amplitude) is 'hexadirectional modulation.'

Canonical hexadirectional analysis and Fourier decomposition

In hexadirectional analysis, the amplitude of polar sinusoids are used as a measure of k-fold rotational symmetry in an angular signal, specifically for the 6th harmonic. This is computed using the following regression:

(1) $r(t) = \beta_0 + \beta_1 * cos(6 * \theta(t)) + \beta_2 * sin(6 * \theta(t)) + \varepsilon(t)$

Which implies (under standard regression assumptions)

(2) $\bar{r}(\theta) = \beta_0 + \beta_1 * cos(6 * \theta) + \beta_2 * sin(6 * \theta)$ where $\bar{r}(\theta) = E[r|\theta]$

Such that

$A_6 = \sqrt{\beta_1^2 + \beta_2^2}$

This is equivalent to the Fourier series for the 6th harmonic:

(3) $\bar{r}(\theta) = a_0 + a_6 e^{i6\theta} + a_{-6} e^{-i6\theta}$, such that $A_6 = 2|a_6|$

When angular sampling is uniform ($\Delta\theta$, samples per θ), both approaches produce the same magnitude A_6, and phase ϕ_6.

(A_6= hexadirectional modulation, ϕ_6 = mean grid orientation)

When directional sampling is uneven (more samples for a given direction and/or directions are not evenly spaced), outputs vary. In the latter case Fourier decomposition requires an explicit interpolation step. Advantageously this explicit interpolation step forces the user to address irregular sampling biases explicitly, as opposed to regression where they can go unnoticed. Another advantage is computational efficiency of the Discrete Fourier Transform, especially when quantifying multiple symmetries, which are calculated simultaneously.

Importance of the spectral perspective

In canonical hexadirectional analysis the 6-period sinusoid regression is treated largely as a standalone model. Analyzing the 6th harmonic on its own is a major pitfall. The magnitude of any single harmonic largely reflects overall signal scale and is only meaningful relative to the remainder of the spectrum, and an appropriate null distribution. Natural signals contribute power across many harmonics. Thus the null expectation of this metric is not zero, but a nonzero, typically nonuniform distribution (Figure 2A, Figure S1A). Specifically the 1/f null distribution is common (f = k in k-symmetry context). Consequently, statistically testing harmonic magnitudes against zero is mis-specified.

Many hexadirectional studies do control for other harmonics/symmetries, however this is done idiosyncratically, typically for some subset of k = 4-9. However, comparing in only a narrow band provides incomplete spectral context which can distort overall inference (Figure S1C). This can be in Figure 2D (Fourier=orange) in which a 3-symmetric signal through a 4-9 band (yellow highlight) appears harmonically as a 6-symmetry.

A spectral perspective also elucidates essential constraints. Sampling-rate (angular bin spacing) and smoothing windows limit which symmetries are detectable, which is not necessarily apparent if not approaching this method from a spectral analysis perspective. Full spectrum decomposition also enables

normalization (see below) and comparability across datasets, and is more interpretable than reporting an unbounded regression coefficient (β).

One notable methodological choice in this work is not to subtract the mean from our signal before fourier decomposition. The reason for this is that we are not using the decomposition purely to describe periodicities in our signal, our goal is more broadly to get a sense of how periodic activity at the micro scale is detected at the macro scale. If the entirety of the symmetric modulation comes down to x number of spikes, we want to know if the mean of the population activity is closer to 10x or 10000x i.e. how big of a modulation should we expect. While in theory not removing the mean can cause spectral leakage in the low symmetries (frequencies). Fortunately in our case, we care only about whole symmetries (6-fold not 6.1-fold), which are exact harmonics of our sampling window (i.e. 2pi/n where n is always an integer), in which case the fourier bases are entirely orthogonal, meaning they are not affected by leakage from the mean.

With the mean included we can more easily relate the magnitude of any given symmetry to the full spectrum of periodic activity in the signal as well as the overall magnitude of the signal itself. In our case we do a simple normalization of the magnitude (amplitude) of a particular symmetry divided by the total sum (including the 0 symmetry which is the signal mean) $\hat{A}_k = \frac{A_k}{\sum A}$ We then express this as a percentage and call it “Signal Contribution". This gives us a sense of the modulation of the signal at a given periodicity relative to the magnitude of the entire signal. It could be argued that a better measure would be power (A_k^2) instead of magnitude. For statistical inference, the power would tell us how much each symmetry contributes to the variance of the angular signal (Persival’s theorem), however this is only in the case if we subtract the mean. Since we are not subtracting the mean, we chose the former measure for the reasons described. Importantly, the choice of using the coefficient magnitude (A_k) also keeps symmetry modulation in the scale of the actual signal (similar to the standard deviation), without squaring the magnitudes (as in the variance), which is easier to intuit. That said, we have observed anecdotally that power, due to the nonlinearity of squaring, can do a better job of dampening noise symmetric modulation when values are normalized between [0 1] as above.

All that said, sinusoidal decomposition is an imperfect metric for rotational symmetry.

Quantifying rotational symmetry with sinusoids

There is an implicit bias in using sinusoid amplitude as a proxy for k-fold rotational-symmetry, which is that the signal is k-periodic sinusoid shaped (square-wave shaped in the case of RSA). This may not be the case, for example when the hexadirectional signal is generated by grid x HD cells with narrow directional tuning. In general, a perfectly k-fold symmetric pattern will have different power in the decomposed k-frequency depending on how well the signal fits a sinusoid. Conversely, the decomposition of an asymmetric signal will have a spectral profile dependent on how well the widths of its peaks fit a k-periodic sinusoid. In other words, the k-component projection of a sinusoid can be driven by one or several strong peaks whose angular positions and/or shape happen to align with that sinusoid. In this case, the signal reflects directional tuning with incidental harmonic structure, not k-symmetric peaks spanning

over 360° (Figure S1D). Demonstrating symmetric activity should require evidence of multiple peaks with approximately k-fold spacing rather than isolated features that merely 'resonate' with a sinusoid.

Symmetric variance

To more parsimoniously measure symmetry in a directional signal, S_θ, we introduce Symmetric Variance (SV), which quantifies how much variance is explained by symmetric grouping, (Figure 2D). This simple, normalized measure works by comparing the fraction of signal variance explained by across-group-variance, when the signal is grouped by coordinates that are equivalent according to the symmetry. While it can be implemented for any symmetry; in this context we use k-fold rotational symmetry.

To quantify the amount of k-fold symmetry in directional signal S_θ, we group the values such that:

$$g_k(\theta) = \{\theta + m\,\frac{360°}{k}\}_{m=0}^{m=k-1}$$

For example to test 3-fold symmetry, we would group the directions [1°,121°, 241°] together.
We then take the mean of each group, and divide the variance across groups by the total signal variance:

$$V_k = \frac{var_\theta(\mathbb{E}_{g_k(\theta)}[S_\theta])}{var(S_\theta)}$$

We then correct this value by the expected reduction of variance, $\frac{\sigma^2}{k}$ if the values in the groups are independent:

$\tilde{V}_k = \frac{V_k - \frac{1}{k}}{1-\frac{1}{k}}$ setting a lower bound of 0, $\tilde{V}_k = min\{0,\ \tilde{V}_k\}$.

Lastly, as an error checking step we compare subsymmetries. For example if a signal is 6-fold symmetric, it must, by definition also be 2- and 3-fold symmetric. To be conservative, we assign the value to the symmetry as the minimum value calculated for the symmetry its sub-symmetries:

$$SV_k = min\,\{\tilde{V}_d : d|k,\ d \neq 1\}\,.$$

The result is a unitless metric between [0 1] that is invariant to phase and agnostic to signal shape. It can be viewed as a simple ANOVA-style variance decomposition, that quantifies the fraction of total angular variance explained by between-group-variance (grouped by symmetry in this case), directly aligning the method with standard variance-based effect size and reliability measures (e.g., ANOVA-η^2 or Intraclass Correlation Coefficient).

In simulation this method appears more robust to noise, and the artifacts related to signal shape mentioned above (Figure 2D).

For a more conservative metric, SV_k^2 , is even more robust to noise. Another advantage of this metric is that since the computation for symmetry with Fourier is fairly different, the two metrics yield fairly different results when the signal is noisy. Consequently another useful metric is $A_k * SV_k$, especially when done for the whole spectrum. While not perfect, it is arguably more parsimonious, at the very least compliments the sinusoid approach when analyzing noisy signals.

Regression betas in hexadirectional analysis

A central measure of hexadirectional analyses in the literature is the contrast of beta estimates of the aligned and misaligned conditions[21], or alternatively, the contrast of the beta estimate of an aligned cosine regressor and baseline[13]. Beta parameter estimates in GLMs can be signed and are unbounded. Negative beta values are not uncommon for the aligned condition for individual participants. However, it is arguably unintuitive how to interpret these negative values (which imply that the preferred mean grid orientation has changed orthogonally between partitions). Instead, a more intuitive approach would be to report the actual preferred angles (the phase of the Fourier decomposition, ϕ_k) of the different data partitions (see for example[21]), as well as the signal magnitudes, because these directly relate to the environments that participants navigated in. Reporting these separately also removes ambiguity about what causes differences in symmetric modulation. When a single beta value is used to express modulation in the case of GLM analysis, it is influenced both by phase alignment and peak magnitudes independently, but typically interpreted as being modulated by phase alignment alone.

Synthesized data

Simulation

The goal of the simulation was to generate a population of MEC neurons firing as a rodent moves around an open-field arena in order to match, and extrapolate beyond the limits of our empirical dataset. We focus on grid cells but also simulate head direction cells, conjunctive grid-x-head direction cells, spatially informative cells and pure noise cells. The ultimate goal being to do a directional analysis of the population signal with ground truth knowledge of individual neuron activity.

We use a stochastic model in which probabilities are sampled to give a spike count over a time interval. Cell populations are any combination of *grid*, *conjunctive* (grid x head direction, hd), *hd*, *place*, and *random* firing cells. While place cells are not typically found in the MEC, other spatially tuned/spatially informative cells are[2,36]. Although we call them "place cells" when considered collectively, in the model they are a proxy for the type of spatially dependent noise added to the grid cell signal from these spatially informative neurons of the MEC. In the model *place* and *pure grid* cells have only a spatial firing probability $p(x, y)$, *hd* cells have only a direction firing probability $p(\theta)$, *conjunctive* cells have a joint probability $p(x, y)\ p(\theta)$, and *random* cells have a uniformly random probability of firing.

Firing is based on a stochastically determined firing rate, which is translated into a Bernoulli spike/no-spike probability of *n* trials where *n* is the firing rate multiplied by time interval. For this study we simulated sampling at 2Hz (somewhere in the range of a very high fidelity BOLD signal), so the time interval was 0.5s. A n-trial Bernoulli distribution is approximated by a Poisson distribution, which to speed up computation we further approximated with a gaussian distribution.

Grid and *place* cells were modeled as 2D normal distributions firing fields based on distance to the location of the field center. For *hd and conjunctive* cells directional firing probability was modeled as circular normal distribution based on circular distance to the tuning angle. If desired, grid patterns were generated such that they could have a random degree of ellipticity as well as a uniform amount of location noise with respect to the center of the field relative to the perfectly geometric pattern. Directional tuning for conjunctive cells was tuned to match the same tuning specificity (mvl) from the empirical distribution of the Gardner et al. 2022[62] dataset (containing only grid and conjunctive grid-x-hd cells) at uniformly random tuning angles. This dataset is a subset of the Vollan et al. 2025[37] dataset which had not been released at the time the model was being built. HD cells had uniform random mvl value from [0.7,1] with a uniformly random tuning angle.

Trajectories were generated as a collection of individual straight segments of fixed length and varying direction. Directions were sampled every n degrees with some added noise to avoid artifacts from sampling an exactly symmetric set of directions. At every direction the starting points of the segments were randomly distributed in an approximately circular shape forming disk shaped sample space collectively.

The overall parameters of the simulations usually matched a typical rodent experiment's, including grid-spacing in the tens of centimeters, and trajectory area of around 1-2 m^2. Path segment length was usually in the 10s to 100s of centimeters, with speed held constant at around 20cm/s, translating to sampling at approximately every 10cm. It should be noted that straight paths of this length are not typical in empirical rodent openfield experiments, and consequently are the main motivation for building this model as they are required to see the hexadirectional signal.

A typical simulation might have segment lengths of 150cm x 50 segment samples per angle x 60 angles samples so ~ 45,000 points sampled per cell. To optimize this we converted as much of these computations as we could to matrix multiplications and performed them on a single GPU with 14GB of VRAM. With this approach we could simulate 1 million cells for a total rodent distance of 4.5 km (~6hr simulated time), in around 20 minutes, with the majority of simulation time determined by the number of cells. We validated the model by generating directional and spatial firing rate maps and checking the statistical distributions of our simulated data to see that we were generating spike trains and rate maps that would seem reasonable in a rodent experiment.

Hybrid approach

Despite developing a fairly detailed model with lots of parameters to explore, when the Vollan et al. 2025[37] dataset became available, we decided that we wanted to draw our conclusions as much from this dataset as possible since it contains a wealth of simultaneously recorded cells in addition to grid cells,

whose complex spatial and directional characteristics could not be replicated with simple stochastic exploration of our computational model's parameter space. However despite having this excellent data to explore, it was imperative to have many long straight trajectory samples in all directions, which as mentioned, the rodents themselves did not provide. For this reason, we essentially lifted our trajectories from the simulation, and instead sampled from the empirically calculated directional $f(\theta_t)$ and spatial $f(x_t, y_t)$ firing maps, which we treated as independent firing-rate profiles whose product defines a separable joint firing-rate model. To correct for biases from the rodents sampling only a subset of the directional and 2D space in the empirical trajectories, we also normalize such that mean firing of the sampled trajectory matched the empirical mean firing rate $\bar{r}$:

$$r(t) = \bar{r}\,\frac{f(x_t,y_t)f(\theta_t)}{\langle f(x,y)f(\theta)\rangle}$$

The assumption that spatial and directional tuning is independent is probably not entirely accurate. For example Gerlei et al. 2020[63] reports that in pure grid direction cells, directional tuning changes per field. We did try more complex models of spatial and directional tuning dynamics to model individual cells, including GLMs and Gaussians processes fitted to the empirical $x, y, \theta, r(t)$, but ultimately we lacked enough data to cover this joint probability space dependently unless we used large spatial and directional bins, which did not yield enough specificity to generate realistic grid cell firing profiles.

Ultimately we decided that using this framework of factorized independent spatial and directional tuning was fairly in line with how these tunings are usually discussed in the field, and more relevantly, how they are utilized to construct the hypotheses that lead to the hexadirectional signal.

In this regime the ratemaps generated from our sampled trajectories match the original rate maps almost exactly, so conceptually we can say that we simply extend these first order dynamics for longer trajectories. That said, we are likely missing some relevant spatial and directional dependence or other higher-order temporal or network dynamics, but we are not aware of any hypotheses related to the hexadirectional signal that rely on these. Notably because we relied on the empirical spatial ratemaps, the length of our segments were still bounded to the confines of the original environment, a ~1.5m square (with the exception of two recordings in a circular environment), and the empirical grid patterns (see Figure 4B middle, x-axis). Lastly we initially treated r(t) as a stochastic value λ in a poisson distribution, but found that with the number of samples we are taking per trajectory, 10s of thousands, this had negligible effect while slowing down the simulation noticeably. Instead stochasticity is achieved by randomly sampling trajectory segments.

Modified grid score

While not central to this study, we made an attempt to better classify grid cells in our ~24k cell database by modifying how we quantify gridness in spatial firing ratemaps. The canonical grid score method[58] extracts a ring out of the rate map autocorrelogram, ideally at the radius and width to match a ring of autocorrelated grid fields. This ring is rotated and correlated/anticorrelated in alternating 30 degree increments. The most important modification to this method we made is to quantify the roundness of these firing fields in the autocorrelated image, and to more precisely identify them to extract a more

accurate ring. We made this change because of the many false positive instances of high grid scores from noise ratemaps we had using the canonical method, the reasons of which are described below. We do this mostly with a rudimentary image processing pipeline.

Methodological reasons for false positives in gridness score

At the conceptual level, the false positives in the standard 'gridness' measure come from over-rewarding radial symmetry (6-fold in this case) which has a generally high chance probability in autocorrelograms, while under rewarding translational symmetry which is a defining characteristic of lattice patterns (the autocorrelation does accomplish this in theory, but it is ultimately washed out in downstream steps as described below). More specifically, these false positives occur from three factors. 1. The relatively small amount of the autocorrelogram that is correlated (area of the ring). 2. The relatively anisotropic pattern (random spatial peaks, not uniform noise) created by the pre-smoothing of the ratemaps and/or the inherent smoothing of the autocorrelation operation. 3. The fundamental mismatch between the geometry of the shape of the spatial bin being correlated (portion of ring when divided by 6, i.e. rounded trapezoid) and the shape of ideal grid fields themselves (ideally circular). At face value, the 30° increment correlation/anticorrelation procedure produces a maximal effect (a combined correlation value of 2) when a 60° degree slice of a ring shaped pattern inverts every 60° degrees. Consequently the part of the grid field that does not fit in the trapezoidal bin systematically detracts from the correlation magnitude. In our simulation of idealized perfect grid cells, this led to maximal grid scores of around 1.5. On the other hand, random ratemaps can often lead to inadvertent 6-fold symmetries, especially given their anisotropic nature, which would regularly lead to grid scores higher than this threshold.

A partial solution with a focus on firing field circularity using image processing

Given the mismatch of the geometry described above, we found that one requirement that was really impactful was identifying circular firing fields in the autocorrelated ratemaps. This eliminated a lot of false positives that arose from the relatively high levels of 6-fold spatial symmetry from autocorrelated, smoothed random firing. We did this by requiring some prior on expected grid field size in the form of a default grid field radius. We start by removing high frequency image noise (salt and pepper etc), and then use a round spatial filter based on this default field radius to enhance larger firing patterns, before autocorrelating the rate map. After this we apply a series of filters to discretize and threshold these larger firing patterns eventually leading to a binary map of large firing and no-firing regions. We next use some morphological operations (binary image processing methods) to clean up the image for small/jagged features. Ultimately we are left with a series of blobs. We then only consider fairly round blobs using the standard area/perimeter circularity measure, $\frac{4\pi A}{P^2}$. We then use the outer and inner radius of these blobs to form our ring, and apply the rest of the standard grid score measure on this binary image (30° increment correlation/anti-correlation). This addition was quite effective in analyzing this dataset, but in reality cannot be described as a universal method. That said, for those wishing to improve grid score, we highly recommend exploring this line of processing.

References:

1. Ranck, J. B. J. Head-direction cells in the deep cell layers of dorsal presubiculum in freely moving rats. in *Soc. Neurosci. Abstr.* 10:599 (1984).
2. Taube, J. S. The head direction signal: origins and sensory-motor integration. *Annual review of neuroscience* **30**, 181–207 (2007).
3. Buzsáki, G. & Moser, E. I. Memory, navigation and theta rhythm in the hippocampal-entorhinal system. *Nature Neuroscience* **16**, 130–138 (2013).
4. Hafting, T., Fyhn, M., Molden, S., Moser, M.-B. & Moser, E. I. Microstructure of a spatial map in the entorhinal cortex. *Nature* **436**, 801–6 (2005).
5. O'Keefe, J. & Dostrovsky, J. The hippocampus as a spatial map: Preliminary evidence from unit activity in the freely-moving rat. *Brain Research* **34**, 171–175 (1971).
6. The Nobel Committee for Physiology or Medicine. The Nobel Prize in Physiology or Medicine 2014 - Prize Announcement. http://www.nobelprize.org/nobel_prizes/medicine/laureates/2014/announcement.html (2014).
7. Dolan, R. J. Neuroimaging of Cognition: Past, Present, and Future. *Neuron* **60**, 496–502 (2008).
8. Berens, P., Logothetis, N. & Tolias, A. Local field potentials, BOLD and spiking activity – relationships and physiological mechanisms. *Nat Prec* 1–1 (2010) doi:10.1038/npre.2010.5216.1.
9. Epp, S. M. *et al.* BOLD signal changes can oppose oxygen metabolism across the human cortex. *Nat Neurosci* 1–12 (2025) doi:10.1038/s41593-025-02132-9.
10. Howarth, C., Mishra, A. & Hall, C. N. More than just summed neuronal activity: how multiple cell types shape the BOLD response. *Philos Trans R Soc Lond B Biol Sci* **376**, 20190630 (2020).
11. Laurent, M.-A. *et al.* A tight relationship between BOLD fMRI activation/deactivation and increase/decrease in single neuron responses in human association cortex. *eLife* **14**, RP104779 (2025).

12. Zhang, X., Pan, W.-J. & Keilholz, S. D. The relationship between BOLD and neural activity arises from temporally sparse events. *NeuroImage* **207**, 116390 (2020).

13. Doeller, C. F., Barry, C. & Burgess, N. Evidence for grid cells in a human memory network. *Nature* **463**, 657–61 (2010).

14. Bao, X. *et al.* Grid-like Neural Representations Support Olfactory Navigation of a Two-Dimensional Odor Space. *Neuron* 1–10 (2019) doi:10.1016/j.neuron.2019.03.034.

15. Bellmund, J. L. S., Deuker, L., Navarro Schröder, T. & Doeller, C. F. Grid-cell representations in mental simulation. *eLife* 1–21 (2016) doi:10.7554/eLife.17089.

16. Constantinescu, A. O., OReilly, J. X. & Behrens, T. E. J. Organizing conceptual knowledge in humans with a gridlike code. *Science* **352**, 1464–1468 (2016).

17. He, Q. & Brown, T. I. Environmental Barriers Disrupt Grid-like Representations in Humans during Navigation. *Current Biology* **29**, 2718–2722 (2019).

18. Horner, A. J., Bisby, J. A., Zotow, E., Bush, D. & Burgess, N. Grid-like Processing of Imagined Navigation. *Current Biology* **26**, 842–847 (2016).

19. Julian, J. B., Keinath, A. T., Frazzetta, G. & Epstein, R. A. Human entorhinal cortex represents visual space using a boundary-anchored grid. *Nature Neuroscience* **21**, 191–194 (2018).

20. Kim, M. & Maguire, E. A. Can we study 3D grid codes non-invasively in the human brain? Methodological considerations and fMRI findings. *NeuroImage* **186**, 667–678 (2019).

21. Kunz, L. *et al.* Reduced grid-cell–like representations in adults at genetic risk for Alzheimer's disease. *Science* **350**, 430–433 (2015).

22. Maidenbaum, S., Miller, J., Stein, J. M. & Jacobs, J. Grid-like hexadirectional modulation of human entorhinal theta oscillations. *Proceedings of the National Academy of Sciences* 201805007 (2018) doi:10.1073/pnas.1805007115.

23. Moon, H.-J. *et al.* Changes in spatial self-consciousness elicit grid cell–like representation in the entorhinal cortex. *Proc Natl Acad Sci U S A* **121**, e2315758121.

24. Nau, M., Navarro Schröder, T., Bellmund, J. L. S. & Doeller, C. F. Hexadirectional coding of visual space in human entorhinal cortex. *Nature Neuroscience* **21**, 188–190 (2018).

25. Park, S. A., Miller, D. S. & Boorman, E. D. Inferences on a multidimensional social hierarchy use a grid-like code. *Nat Neurosci* **24**, 1292–1301 (2021).

26. Peters-Founshtein, G., Dafni-Merom, A., Monsa, R. & Arzy, S. Evidence for grid-cell-like activity in the time domain. *Neuropsychologia* **198**, 108878 (2024).

27. Stangl, M. *et al.* Compromised Grid-Cell-like Representations in Old Age as a Key Mechanism to Explain Age-Related Navigational Deficits. *Current Biology* **28**, 1108-1115.e6 (2018).

28. Staudigl, T. *et al.* Hexadirectional Modulation of High-Frequency Electrophysiological Activity in the Human Anterior Medial Temporal Lobe Maps Visual Space. *Current Biology* **28**, 3325-3329.e4 (2018).

29. Wagner, I. C. *et al.* Entorhinal grid-like codes and time-locked network dynamics track others navigating through space. *Nat Commun* **14**, 231 (2023).

30. Xiao, Z. *et al.* Human hippocampal ripples align new experiences with a grid-like schema. *Neuron* **113**, 3661-3672.e4 (2025).

31. Graichen, L. P. *et al.* Entorhinal grid-like codes for visual space during memory formation. *Nat Commun* **16**, 9247 (2025).

32. Tavares, R. M. *et al.* A Map for Social Navigation in the Human Brain. *Neuron* **87**, 231–243 (2015).

33. Kransberg, J. *et al.* Failure to replicate detection of grid-cell like representations in human fMRI. *Alzheimer's & Dementia* **20**, e086080 (2024).

34. Kunz, L. *et al.* Mesoscopic Neural Representations in Spatial Navigation. *Trends in Cognitive Sciences* 1–16 (2019) doi:10.1016/j.tics.2019.04.011.

35. Bin Khalid, I., Reifenstein, E. T., Auer, N., Kunz, L. & Kempter, R. Quantitative modeling of the emergence of macroscopic grid-like representations. *eLife* **13**, e85742 (2024).

36. Obenhaus, H. A. *et al.* Functional network topography of the medial entorhinal cortex. *Proceedings of the National Academy of Sciences* **119**, e2121655119 (2022).

37. Vollan, A. Z., Gardner, R. J., Moser, M.-B. & Moser, E. I. Left–right-alternating theta sweeps in entorhinal–hippocampal maps of space. *Nature* **639**, 995–1005 (2025).

38. Slettmoen, T. Mechanisms of Six-Fold Symmetry in fMRI BOLD-Signal: An Analysis of a Large Grid Cell Dataset. (NTNU, 2020).

39. Stensola, T., Stensola, H., Moser, M.-B. & Moser, E. I. Shearing-induced asymmetry in entorhinal grid cells. *Nature* **518**, 207–212 (2015).

40. Mechelli, A., Price, C. J. & Friston, K. J. Nonlinear Coupling between Evoked rCBF and BOLD Signals: A Simulation Study of Hemodynamic Responses. *NeuroImage* **14**, 862–872 (2001).

41. Friston, K. J., Mechelli, A., Turner, R. & Price, C. J. Nonlinear Responses in fMRI: The Balloon Model, Volterra Kernels, and Other Hemodynamics. *NeuroImage* **12**, 466–477 (2000).

42. Toyoda, H. *et al.* Source of nonlinearity of the BOLD response revealed by simultaneous fMRI and NIRS. *NeuroImage* **39**, 997–1013 (2008).

43. Gagliano, G. *et al.* Non-Linear Frequency Dependence of Neurovascular Coupling in the Cerebellar Cortex Implies Vasodilation–Vasoconstriction Competition. *Cells* **11**, 1047 (2022).

44. Attwell, D. *et al.* Glial and neuronal control of brain blood flow. *Nature* **468**, 232–243 (2010).

45. Blazquez Freches, G., Chavarrias, C. & Shemesh, N. BOLD-fMRI in the mouse auditory pathway. *Neuroimage* **165**, 265–277 (2018).

46. Heinsen, H. *et al.* Quantitative investigations on the human entorhinal area: left-right asymmetry and age-related changes. *Anat Embryol* **190**, 181–194 (1994).

47. Price, J. L. *et al.* Neuron Number in the Entorhinal Cortex and CA1 in Preclinical Alzheimer Disease. *Arch Neurol* **58**, 1395 (2001).

48. Gómez-Isla, T. *et al.* Profound Loss of Layer II Entorhinal Cortex Neurons Occurs in Very Mild Alzheimer's Disease. *J. Neurosci.* **16**, 4491–4500 (1996).

49. Syversen, I. F. *et al.* A combined DTI-fMRI approach for optimizing the delineation of posteromedial versus anterolateral entorhinal cortex. *Hippocampus* **34**, 659–672 (2024).

50. Maass, A., Berron, D., Libby, L., Ranganath, C. & Düzel, E. Functional subregions of the human entorhinal cortex. *eLife* **4**, 1–20 (2015).

51. Navarro Schröder, T., Haak, K. V., Zaragoza Jimenez, N. I., Beckmann, C. F. & Doeller, C. F. Functional topography of the human entorhinal cortex. *eLife* **4**, 1–17 (2015).

52. Syversen, I. F. *et al.* Structural connectivity-based segmentation of the human entorhinal cortex. *NeuroImage* **245**, 118723 (2021).

53. Stangl, M. *et al.* Compromised grid-cell-like representations in old age as a key mechanism to explain age-related navigational deficits. *Current Biology* **28**, 1108–1115 (2018).

54. Botvinik-Nezer, R. *et al.* Variability in the analysis of a single neuroimaging dataset by many teams. *Nature* **582**, 84–88 (2020).

55. Turner, B. O., Paul, E. J., Miller, M. B. & Barbey, A. K. Small sample sizes reduce the replicability of task-based fMRI studies. *Communications Biology* **1**, (2018).

56. Gu, Y. *et al.* A Map-like Micro-Organization of Grid Cells in the Medial Entorhinal Cortex. *Cell* **175**, 736-750.e30 (2018).

57. Sargolini, F. *et al.* Conjunctive representation of position, direction, and velocity in entorhinal cortex. *Science (New York, N.Y.)* **312**, 758–62 (2006).

58. Stensola, H. *et al.* The entorhinal grid map is discretized. *Nature* **492**, 72–8 (2012).

59. Yoon, K., Lewallen, S., Kinkhabwala, A. A., Tank, D. W. & Fiete, I. R. Grid Cell Responses in 1D Environments Assessed as Slices through a 2D Lattice. *Neuron* **89**, 1086–1099 (2016).

60. Esteban, O. *et al.* fMRIPrep: a robust preprocessing pipeline for functional MRI. *Nat Methods* **16**, 111–116 (2019).

61. Barry, C. & Burgess, N. To be a Grid Cell: Shuffling procedures for determining “Gridness”. 230250 Preprint at https://doi.org/10.1101/230250 (2017).

62. Gardner, R. J. *et al.* Toroidal topology of population activity in grid cells. *Nature* **602**, 123–128 (2022).

63. Gerlei, K. *et al.* Grid cells are modulated by local head direction. *Nat Commun* **11**, 4228 (2020).